Fort Hays State University

FHSU Scholars Repository

Chemistry Faculty Publications

Chemistry

8-27-2015

HOMO−LUMO energy gap control in platinum(ii) biphenyl complexes containing 2,2'-bipyridine ligands

D. Paul Rillema
Wichita State University, paul.rillema@wichita.edu

Stanislav R. Stoyanov
University of Alberta, stoyanov@yalberta.ca

Arvin Cruz
Fort Hays State University, ajcruz2@fhsu.edu

Huy Nguyen
Wichita State University

Curtis Moore
Fort hays State University

See next page for additional authors

Follow this and additional works at: https://scholars.fhsu.edu/chemistry_facpubs

Part of the Chemistry Commons

Recommended Citation

Authors

D. Paul Rillema, Stanislav R. Stoyanov, Arvin Cruz, Huy Nguyen, Curtis Moore, Wei Huang, Khamis Siam, Ali Jehan, and Venugopal KomReddy

HOMO-LUMO Energy Gap Control in Platinum(II) Biphenyl Complexes Containing 2,2'-Bipyridine Ligands

D. Paul Rillema[1]*, Stanislav R. Stoyanov[2,3,4,]*, Arvin J. Cruz[5], Huy Nguyen[1], Curtis Moore[6], Wei Huang[1], Khamis Siam[7], Ali Jehan[1] and Venugopal KomReddy[1]

[1]Department of Chemistry, Wichita State University, Wichita, KS 67260, USA

[2]National Institute for Nanotechnology, 11421 Saskatchewan Drive NW, Edmonton, Alberta, T6G 2M9, Canada

[3]Department of Chemical and Materials Engineering, University of Alberta, Edmonton, Alberta, T6G 2V4, Canada

[4]Department of Mechanical Engineering, University of Alberta, Edmonton, Alberta, T6G 2G3, Canada

[5]Department of Chemistry, Fort Hays State University, Hays, KS 67601, USA

[6]Crystallography Lab, University of California, San Diego, La Jolla, CA 92093

[7]Department of Chemistry, Pittsburg State University, Pittsburg, KS 66762, USA

* Corresponding authors. E-mail: **paul.rillema@wichita.edu; stoyanov@ualberta.ca**

1

Abstract

A series of platinum(II) biphenyl 2,2'-bipyridine complexes containing electron-donating and electron-withdrawing moieties on the 4 and 4' positions of the bipyridine ligand exhibit emission from excited states in the 600 nm region of the spectrum upon excitation in the metal-to-ligand charge transfer transition located near 450 nm. These complexes are distorted from planarity based on both single crystal structure determinations and density functional theory (DFT) calculations of isolated molecules in acetonitrile. The DFT also reveals the geometry of the lowest-lying triplet state (LLTS) of each complex that is important for emission behavior. The LLTS are assigned based on the electron spin density distributions and correlated with the singlet excited states to understand the mechanism of electronic excitation and relaxation. Time-dependent DFT calculations are performed to compute the singlet excited state energies of these complexes so as to help interpret their UV-Vis absorption spectra. Computational and experimental results, including absorption and emission energy maxima, electrochemical reduction potentials, LLTS, singlet excited states, and LUMO and HOMO energies, exhibit linear correlations with the Hammett constants for para-substituents σ_p. These correlations are employed to screen complexes that have not yet been synthesized. The correlation analysis indicates that electronic structure and the HOMO-LUMO energy gap in Pt(II) complexes can be effectively controlled using electron-donating and electron-withdrawing moieties covalently bonded to the ligands. The information presented in this paper provides analysis and better understanding of the fundamental electronic and thermodynamic behavior of these complexes and could be used to design systems with specific applications.

Figure and wording for the Table of Contents:
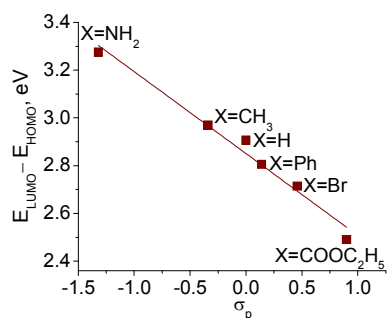
Electronic properties including the HOMO-LUMO energy gap in Pt(II) complexes can be effectively controlled using electron-donating and electron-withdrawing moieties covalently bonded to the ligands.

Introduction

Square planar complexes of platinum(II) containing a biphenyl dianion ligand and the other ligand being diimine,[1,2,3,4] phosphine,[5] pyridyl,[6] acetonitrile,[6,7] CO,[8,9] or diene,[10,11] as well as complexes containing η^1-biphenyl monoanion[12] and phenylpyridine[13,14] ligands have been attractive to researchers due to potential applications in photocatalytic,[5,15] optoelectronic,[16,17,18] chemosensory,[1,13] and biomedical imaging devices.[14] This research interest is largely due to the significant Stokes shift, tunable emission wavelengths and high photoluminescence efficiency of these compounds.[19] Previously reported Pt(II)-biphenyl complexes containing 2,2'-bipyridine and 1,10-phenanthroline ligands exhibit broad absorption in the visible region of the solar spectrum in both solution and solid state and emit in the visible light region.[1,2] The photophysical properties of these complexes are associated with the metal-to-ligand charge transfer (MLCT) transition that has been extensively studied by UV-Vis absorption and emission spectroscopies.[2] The emission under dilute conditions for these complexes has been assigned primarily as triplet MLCT (^{3}MLCT) and triplet ligand-centered (^{3}LC).[1,2,4,7,11] According to Kasha's rule, fast decay occurs in the triplet manifold to the lowest-lying triplet state (LLTS), which is the emissive state.[20] Despite extensive exploration with the most advanced spectroscopic techniques, there is no solid evidence showing violation of this rule except for case of photoisomerization[21] and at low temperature due to constrained thermal relaxation.[22]

Density functional theory (DFT)[23] calculations have been extensively employed to study the geometry and electronic structure of square planar transition metal complexes of Pt(II),[17,24,25,26,27] Ni(II),[28,29] and Pd(II)[30,31] as well as those embedded in doped carbon nanocones, nanotubes and fullerenes.[32] In the latter study, DFT has revealed extended metallic states that participate in axial coordination of ions controlled by using external electric field, as highly

relevant to scanning tunneling microscopy and nanoelectronic devices.[32]   The bathochromic shifts of the phosphorescence emission spectra of $[Pt_2(\mu\text{-}P_2O_5H_2)_4]^{4-}$ and $Pt(bph)(CO)_2$ have been attributed to Pt-Pt bonding and stacking of these square-planar complexes in the triplet state.[17,26,33]   The mechanism of axial coordination to Ni(II) porphyrins upon excitation from singlet ground to triplet excited states in the presence of pyridinic ligands has also been investigated.[28]

The time-dependent DFT method (TD-DFT)[34] allows one to compute singlet and triplet excited state energies[26,35] as well as to optimize the geometry of excited electronic states.[36,37] The photophysical properties of Ru(II),[17,38] Fe(II),[39] and Re(I) complexes[16,40] have been investigated to provide spectral assignments and detailed interpretation of   electronic transitions.[41,42] In a recent report, Zhekova *et al.* have evaluated the DFT and TD-DFT methods with respect to the prediction of excitation energies of tetrahedral Cu(II) complexes.[43]   Also, Escudero and Thiel have investigated the emission behavior of a cyclometalated Pt(II) complex using these methods.[37]

In this paper, [Pt(bph)(4,4'-X₂bpy)] complexes, where bph is the 2,2'-biphenyl dianion and bpy is 2,2'-bipyridine functionalized with electron donating and electron withdrawing substituents in the 4,4'-positions (listed in Table 1) are correlated experimentally and theoretically with their ground state and excited state properties., Earlier, Cummings and Eisenberg reported excited state properties of platinum(II) diimine dithiolate complexes could be tuned with various functionalized diimine ligands.[44] Tuning of HOMO and LUMO energies by using electron-donating or electron-withdrawing substituents was used for iridium(III) complexes[45] and for the design of dyes for dye sensitized solar cells.[46]   Here we examine electronic and thermodynamic free energy correlations guided by quantum chemistry treatments

involving DFT and TD-DFT. The electronic absorption and emission spectra are correlated with calculated singlet excited states and LLTS, respectively. The energies of the lowest unoccupied molecular orbitals (LUMO) computed using DFT are correlated with thermodynamic quantities, such as electrode potentials. These correlations provide insights into the spontaneity and reversibility of redox processes as related to the nature of excited states. The substituents are correlated based on the Hammett constants for para substitution[47] σ_p that are listed in Table 1.

Table 1. Hammett Constants for Para Substitution[48] (σ_p) in Phenyl Groups

Substituent	σ_p per substituent	σ_p for two substituents
NH_2	-0.66	-1.32
CH_3	-0.17	-0.34
H	0.00	0.00
C_6H_5	+0.07	+0.14
Br	+0.23	+0.46
$COOC_2H_5$	+0.45	+0.90

Experimental Section

Materials All syntheses were performed under a dry and oxygen-free nitrogen atmosphere using standard Schlenk-tube techniques. [Pt(bph)(C$_2$H$_5$)$_2$S]$_2$ was prepared as described.[49,50,51] Methylene chloride and hexanes were purchased from Fisher Scientific and were used as received. Anhydrous diethyl ether (99.7%) was used as received from Aldrich. All the diimine ligands were commercially purchased and used as received. Fluka was the source of tetrabutylammonium hexafluorophosphate (TBAPF$_6$).

Instrumentation and Physical Measurements IR spectra were acquired using a Nicolet Avatar 360 FT-IR spectrophotometer. Proton NMR spectra were obtained using a Varian Inova 400 FT-NMR spectrometer. Elemental (C, H, & N) analysis was performed by Columbia Analytical

Services, Tucson, AZ. An EG&G PAR Model 263A potentiostat/galvanostat was used to obtain the cyclic and differential-pulse voltammograms. The measurements were carried out in a typical H-cell using a platinum disk working electrode, a platinum wire counter electrode, and a $Ag/AgNO_3$ reference electrode in dichloromethane. The supporting electrolyte used was 0.1 M tetrabutylammonium hexafluorophosphate ($TBAPF_6$). Ferrocene was added as the reference. Absorption profile and extinction studies were carried out using an OLIS Cary 14 UV/Visible/NIR double beam spectrophotometer. All solution samples were prepared using spectral grade acetonitrile or freshly distilled butyronitrile.

Emission spectra, excitation spectra and emission lifetimes were obtained using a FL3-2iHR Nanolog spectrometer from Horiba Jobin Yvon Technologies. Solutions with an absorbance of ~0.1 at the λ_{max} of each complex in butyronitrile were placed in Pyrex tubes (5mm, OD; 3 mm ID) and freeze-pump-thaw degassed. After the final degassing, the glassy samples were placed in a Dewar located in the cavity of the spectrometer and maintained at 77 K during measurements. Emission spectra were collected at λ_{max} of the MLCT bands; excitation spectra were obtained at the emission maximum for each compound. A NanoLED-460 pulsed diode light source was used in all lifetime decay determinations. In this case the excitation wavelength used was set to 457 nm – the absorption maximum for the NanoLED-460 light source. Emission curve-fittings were performed using the Origin Pro 8 program via non-linear curve-fitting modes.

Computational Technique

Method Exploration For geometry optimization of the complexes, we evaluated the performance of the hybrid exchange-correlation density functionals B3LYP,[52] PBE0 (keyword PBE1PBE),[53,54] PW91 (keyword PW91PW91),[55,56,57] and B3PW91 (keyword BPBE and internal

options) as implemented in the Gaussian 09 computational chemistry software.[58] These

functionals were evaluated with respect to their capability to produce both the geometry, as in the

X-ray diffraction (XRD) results, and excited states, as in the absorption spectra maxima. The Pt-

N bond length, overestimated by 0.02-0.10 Å by the functionals, was selected as the geometry

optimization performance criterion. The rest of the geometry parameters were in a very good

agreement with the X-ray diffraction results. We found that the B3LYP predicted excited state

energies and PBE0 yielded optimized geometries in a very good agreement with the absorption

spectra maxima and XRD results, respectively, as reported in Supporting Information Tables S1

and S2 and Figure S1. The metal-ligand bond length over-estimation of B3LYP has been noted

previously and reported elsewhere.[16,59] The PBE0 functional gave optimized geometries in a

good agreement with XRD, but predicted excited state energies substantially lower than the

absorption band energies. It is possible to calibrate excited state energies with respect to an

experimental set of absorption spectra maxima, as we have shown previously.[28] However; this

requires an extensive calibration set. Here, we employed the Becke's 3-parameter hybrid

functional with non-local exchange term of Becke, the local correlation term of Vosko, Wilk and

Nusair (VWN),[60] (as in B3LYP) as well as the non-local correlation of Perdew, Burke and

Ernzerhof (PBE),[53] (as in PBE0) and referred to it in the text as B3PBE. This functional yields

metal-ligand distances and singlet excited states in good agreement with PBE0 and B3LYP

functionals, respectively, due to the favorable combination of non-local exchange and correlation

terms.

Computational Details The geometries were optimized in acetonitrile solvent using the

conductor-like polarizable continuum model (CPCM) for solvation.[61,62] The electronic singlet

ground state (SGS) and LLTS for each complex were fully optimized using restricted singlet and

unrestricted triplet B3PBE, respectively. After each geometry optimization, the second-order force constant matrix was calculated to confirm that the optimized geometry was a true minimum on the potential energy surface. The Mayer bond order analysis[63] was employed to analyze bonding. No symmetry restrictions were imposed during geometry optimization. The initial structures were taken from the XRD files, where available, and the rest were prepared by addition of methyl and phenyl groups.

For excited state calculations, we employed the tandem of non-equilibrium TD-DFT[64,65] and CPCM methods, as implemented in the Gaussian 09 software.[58] Forty singlet excited-states were computed in acetonitrile solvent based on the respective SGS geometries optimized in acetonitrile using the CPCM method for Pt(bph)(X$_2$bpy), X = NH$_2$, Me, H, Br, NO$_2$ and CN. Sixty singlet excited-states were computed for the complexes containing Ph and COOC$_2$H$_5$ groups. This tandem approach adds a self-consistent reaction field around the solute and employs a linear response form for calculation of the excited states.[61,66] The excited state energies computed using the TD-DFT/CPCM method correlate linearly with experimental UV-Vis spectra, as we[67,28] and others have shown.[68,69]

The all-electron triple-ζ TZVP basis set (keyword Def2TZVP) was applied for H, C, N, and O atoms.[70] The QZV effective core potentials were used for the Pt and Br atom cores.[70] The quadruple-ζ QZVP basis set was applied for the valence shells of Pt and Br atoms.[70] This combination of basis sets, referred in the text as TZVP-QZV-P, is the largest tractable computationally for our complexes and resources. The GaussView 4.1 visualization software was used to generate the molecular orbital and spin density isosurfaces.

Preparation of Compounds

(1) Pt(bph)(4,4'-Me₂bpy)   A solution of 4,4'-dimethylbipyridine (46 mg, 0.25 mmol) in methylene chloride (10 mL) was added drop-wise to a solution of [Pt(bph)(C₂H₅)₂S]₂ (100 mg, 0.114 mmol) in methylene chloride (20 mL) under continuous stirring.   The brown colored reaction mixture was allowed to stir at room temperature for half an hour, rotary-evaporated to about 10 mL and added drop-wise to 500 mL hexanes.   The brown colored precipitate was isolated, vacuum filtered and washed with ether. Yield: 66 mg (50%) Anal. Calcd for $C_{24}H_{20}N_2Pt$: C, 54.23; H, 3.79; N, 5.27. Found for $C_{24}H_{20}N_2Pt$: C, 53.94; H, 4.20; N, 5.25. IR (KBr pellet): 3040, 1616, 1417, 1034, 830, 739, 521 cm⁻¹. ¹H NMR (CDCl₃): δ ppm 9.39 (d, 2H, J = 5.6 Hz), 7.84 (s, 2H), 7.43 (d, 2H, J = 5.6 Hz), 7.42 (dd, 2H, J = 6.8, 2.0 Hz), 7.38 (dd, 2H, J = 6.8, 2.0 Hz), 7.00 (td, 2H, J = 6.8, 2.0 Hz), 6.94 (td, 2H, J = 6.8, 2.0 Hz), 2.41 (s, 6H).

(2) Pt(bph)(4,4'-Ph₂bpy)·3H₂O Both 4,4'-diphenylbipyridine (18 mg, 0.06 mmol) and [Pt(bph)(C₂H₅)₂S]₂ (25 mg, 0.03 mmol) were added to a round-bottomed flask with a stir bar. Then 5 mL of dichloromethane was added and the mixture was allowed to stir at 40 C for 3 h. The solution was then filtered to remove solid impurities and the filtrate was evaporated to dryness. The solid was redissolved in a small amount of methylene chloride and added to ether to precipitate the compound. The precipitate was removed by vacuum filtration, washed with ether and dried under vacuum. It was then dissolved in methylene chloride and passed over a silica gel column for purification. Yield: 20 mg (51%) Anal. Calcd for $C_{34}H_{32}N_2O_3Pt$: C, 57.38; H, 4.53; N, 3.94. Found for $C_{34}H_{32}N_2O_3Pt$: C, 57.49; H, 3.71; N, 3.96. IR (KBr pellet): 3043, 1610, 1580, 1466, 1412, 1054, 761, 740, 731, 693 cm⁻¹. ¹H NMR (CDCl₃): δ ppm 9.58 (d, 2H, J = 5.6 Hz), 8.29 (d, 2H, J = 1.6 Hz), 7.75 (m, 10H), 7.55 (dd, 2H, J = 5.6, 1.6 Hz), 7.47 (dd, 2H, J = 6.8, 2.0 Hz), 7.34 (dd, 2H, J = 6.8, 2.0 Hz), 6.97 (m, 4H, J = 6.8, 2.0 Hz).

(3) Pt(bph)(4,4'-(NH$_2$)$_2$bpy)·2H$_2$O   Both 4,4'-diaminobipyridine (11 mg, 0.06 mmol) and [Pt(bph)(C$_2$H$_5$)$_2$S]$_2$ (25 mg, 0.03 mmol) were added to a round-bottomed flask with a stir bar. Then 5 mL of dichloromethane was added and the mixture was allowed to stir at 40 C for 3 h. During this time a yellow precipitate formed.   The solid was removed by vacuum filtration, washed with ether and dried under vacuum.   Yellow needles were obtained by recrystallization in methanol. Yield: 17 mg (63%) Anal. Calcd for C$_{22}$H$_{22}$N$_4$O$_2$Pt: C, 46.40; H, 3.89; N, 9.84. Found for C$_{22}$H$_{22}$N$_4$O$_2$Pt: C, 46.30; H, 3.97; N, 9.62. IR (KBr pellet): 3043, 1610, 1580, 1466, 1412, 1054, 761, 740, 731, 693 cm^{-1}. ^{1}H-NMR (DMSO): δ ppm 8.68 (d, 2H, J = 5.6 Hz), 7.30 (dd, 2H, J =5.6, 1.6 Hz), 7.24 (d, 2H, J =5.6), 7.16 (dd, 2H, J = 6.8, 2.0 Hz), 6.99 (d, 2H, J = 6.8), 6.81 (td, 2H, J = 6.8, 2.0 Hz), 6.75 (m, 2H, J = 6.8, 2.0 Hz).

(4) Pt(bph)(4,4'-Br$_2$bpy)·5H$_2$O   Both 4,4'-dibromobipyridine (19 mg, 0.06 mmol) and [Pt(bph)(C$_2$H$_5$)$_2$S]$_2$ (25 mg, 0.03 mmol) were added to a round-bottomed flask with a stir bar. Then 5 mL of dichloromethane was added and the mixture was allowed to stir at 40 C for 3 h. The orange color precipitate was isolated and washed with ether. Yield: 18 mg (48%) Anal. Calcd for C$_{22}$H$_{24}$N$_2$O$_5$Br$_2$Pt: C, 35.17; H, 3.22; N, 3.73. Found for C$_{22}$H$_{24}$N$_2$O$_5$Br$_2$Pt: C, 35.00; H, 2.87; N, 3.67. IR (KBr pellet): 3043, 1610, 1580, 1466, 1412, 1054, 761, 740, 731, 693 cm^{-1}. ^{1}H-NMR (CDCl$_3$): δ ppm 9.42 (d, 2H, J = 5.6 Hz), 8.16 (d, 2H, J = 5.6 Hz), 7.75 (dd, 2H, J = 5.6, 1.6), 7.31 (dd, 2H, J = 6.8, 2.0 Hz), 7.17 (dd, 2H, J = 6.8, 2.0 Hz), 6.98 (dd, 2H, J = 6.8, 2.0 Hz), 6.89 (dd, 2H, J = 6.8, 2.0 Hz).

(5) Pt(bph)(4,4'-(COOC$_2$H$_5$)$_2$bpy)   A solution of 4,4'-diethylesterbipyridine (75 mg, 0.25 mmol) in methylene chloride (10 mL) was added drop-wise to a solution of [Pt(bph)(C$_2$H$_5$)$_2$S]$_2$ (100 mg, 0.114 mmol) in methylene chloride (20 mL) under continuous stirring.   The reaction mixture was stirred at room temperature for half an hour and then rotary-evaporated to reduce its

volume to about 10 mL. The purple crystals that formed were removed by vacuum filtration, washed with ether and dried under vacuum. Yield: 81mg (50%) Anal. Calcd for $C_{28}H_{28}N_2O_4Pt$: C, 51.61; H, 4.33; N, 4.30. Found for $C_{28}H_{28}N_2O_4Pt$: C, 52.12; H, 4.11; N, 4.36. IR (KBr pellet): 3038, 2984, 1731, 1365, 1326, 1252, 1022, 761, 734 cm^{-1}. ^{1}H-NMR (CD_2Cl_3): δ ppm 9.40 (d, 2H, J = 5.6 Hz), 8.20 (d, 2H, J = 1.6 Hz), 7.83 (dd, 2H, J = 5.6, 1.6 Hz), 7.09 (dd, 2H, J = 7.2, 2.0 Hz), 7.02 (dd, 2H, J = 7.2, 2.0 Hz), 6.78 (td, 2H, J = 7.2, 2.0 Hz), 6.58 (td, 2H, J = 7.2, 2.0 Hz), 4.49 (q, 4H, J = 7.2 Hz), 1.51 (t, 6H, J = 7.2 Hz).

Results

X-Ray Diffraction Crystallography Determination

The single crystal X-ray diffraction studies were carried out on a Bruker Kappa APEX-II CCD diffractometer equipped with Mo K$_\alpha$ radiation (λ = 0.71073 Å).[71] Crystals were mounted on a Cryoloop with Paratone-n oil. Data were collected in a nitrogen gas stream at 100 or150 K using ϕ and ϖ scans. Crystal-to-detector distance was 45 or 50 mm and exposure time was 5 or 10 seconds per frame using a scan width of 0.5 or 1.0°. Data collection was ~100% complete to 25.00° in θ for each structure. The data were integrated using the Bruker SAINT software program and scaled using the SADABS software program.[71] Solution by direct methods (SHELXS or SHELXT) produced a complete phasing model consistent with the proposed structure. Crystallographic determination data for the compounds are collected in Table 2 and ORTEP diagrams are provided with thermal ellipsoids drawn at the 50% probability level in Figure 1.

All nonhydrogen atoms were refined anisotropically by full-matrix least-squares (SHELXL-2014). All hydrogen atoms were placed using a riding model. Their positions were

constrained relative to their parent atom using the appropriate HFIX command in SHELXL-2014. The Pt(bph)(4,4'-Me$_2$bpy) complex sits on a general position in the monoclinic space group $P2_1/n$; Pt(bph)(4,4'-Br$_2$bpy) sits on a general position in an orthorhombic space group *Pbca* and Pt(bph)(4,4'-(COOC$_2$H$_5$)$_2$bpy) on a general position in the monoclinic space group *C2/c.*

Table 2. X-ray Diffraction Crystallographic Determination of the Compounds

Identification code	Pt(bph)(4,4'-Me$_2$bpy)	Pt(bph)(4,4'-Br$_2$bpy)	Pt(bph)(4,4'-(COOC$_2$H$_5$)$_2$bpy)
Empirical formula	C$_{23}$H$_{20}$N$_2$Pt$_1$• CH$_2$Cl$_2$	C$_{22}$H$_{14}$Br$_2$N$_2$Pt	C$_{28}$H$_{24}$N$_2$O$_4$Pt$_1$
Formula weight	616.44	661.26	647.58
Temperature	150 K	100 K	150 K
Wavelength	0.71073 Å	0.71073	0.71073 Å
Crystal system	Monoclinic	Orthorhombic	Monoclinic
Space group	$P2_1/n$	Pbca	C2/c
Unit cell dimensions	a = 13.7375(5) Å	a = 7.2532(7) Å	a = 22.3019(11) Å
	b = 9.7822(4) Å	b = 20.093(4) Å	b = 7.1519(4) Å
	c = 17.1526(7) Å	c = 24.757(6) Å	c = 31.0906(15) Å
	α = 90°	α = 90°	α = 90°
	β = 111.300(2)°	β = 90°	β = 105.466(3) °
	γ = 90°	γ = 90°	γ = 90°
Volume	2147.56(15) Å^3	3608.0(14) Å^3	4779.4(4) Å3
Z	4	8	8
Calculated density	1.907 g/cm^3	2.435 g/cm^3	1.800 g/cm3
Absorption coefficient	6.798 mm^{-1}	12.217 mm^{-1}	5.910 mm-1
F(000)	1192	2464	2528
Crystal size	0.33 x 0.23 x 0.04 mm	0.153 x 0.01 x 0.008 mm	0.33 x 0.25 x 0.18 mm
Crystal habit	Plate	Needle	Plate
Crystal color	Clear Light Red	Orange	Lustrous Dark Purple
θ range for data	1.64^o to 26.00^o	2.027^o to 26.428^o	3.40^o to 26.00^o

collection

Limiting indices	$-16 \leq h \leq 16$ $-12 \leq k \leq 12$ $-21 \leq l \leq 21$	$-5 \leq h \leq 9$ $-17 \leq k \leq 25$ $-29 \leq l \leq 30$	$-27 \leq h \leq 27$ $-8 \leq k \leq 8$ $-38 \leq l \leq 38$
Reflections collected / unique	51173 / 4209 [R(int) = 0.0330]	18727/3689 [R(int) = 0.0726]	54008 / 4700 [R(int) = 0.0472]
Completeness to $\theta = 26.00$	100 %	99.9%	99.8 %
Refinement method	Full-matrix least-squares on F^2	Full-matrix least-squares on F^2	Full-matrix least-squares on F^2
Data / restraints / parameters	4209 / 0 / 273	3689/ 0 /244	4700 / 0 / 318
Refinement threshold	$I > 2\sigma(I)$]	$I > 2\sigma(I)$]	$I > 2\sigma(I)$]
Data > threshold	3865		4351
Goodness-of-fit on F^2	1.404	1.036	1.163
Final R indices [$I > 2\sigma(I)$]	R1 = 0.0157, wR2 = 0.0546	R1 = 0.0379, wR2 = 0.0644	R1 = 0.0235, wR2 = 0.0571
R indices (all data)	R1 = 0.0221, wR2 = 0.0923	R1 = 0.0580, wR2 = 0.0703	R1 = 0.0262, wR2 = 0.0584
Largest diff. peak and hole	0.966 and -1.180 e$^-$ Å^{-3}	0.821 and -1.138 e$^-$ Å^{-3}	1.379 and -2.170 e$^-$ Å^{-3}

Pt(bph)(4,4'-Me$_2$bpy)   Pt(bph)(4,4'-Br$_2$bpy)   Pt(bph)(4,4'-(COOC$_2$H$_5$)$_2$bpy)
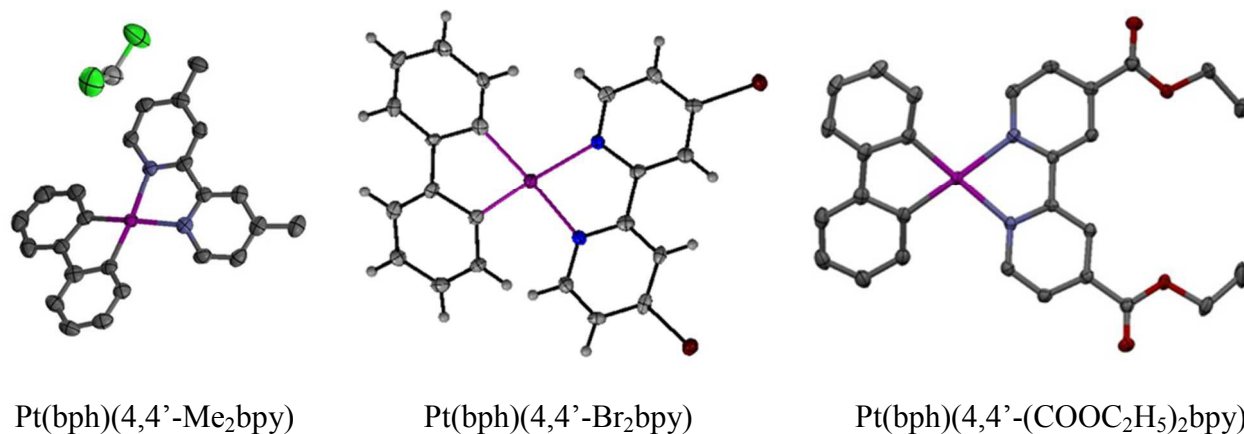
Figure 1. ORTEP diagrams of the complexes Pt(bph)(4,4'-Me$_2$bpy), Pt(bph)(4,4'-Br$_2$bpy) and Pt(bph)(4,4'-(COOC$_2$H$_5$)$_2$bpy).

14

Selected bond distances and angles measured using XRD for single crystals are listed in Table 3. The results show that the Pt-N bonds are longer than the Pt-C bonds by ~0.10-0.12 Å. The C-Pt-C bite angles are ~80° and the N-Pt-N bite angles are 3° smaller at 77°. The torsion angle between the best-fit planes of the biphenyl and 4,4'-bipyridine moieties, referred to as bpy-bph, is particularly important for the evaluation of distortion of these pseudo square-planar complexes from planarity. The bpy-bph torsion angles in the crystal structures of Pt(bph)(Me$_2$bpy), Pt(bph)(4,4'-Br$_2$bpy) and Pt(bph)(4,4'-(COOC$_2$H$_5$)$_2$bpy) are close to that of the previously reported Pt(bph)(bpy)[8] complex, highlighting the X-configuration characteristic to these distorted pseudo square-planar complexes of Pt(II).[1] It is important to note that Pt(bph)(4,4'-Br$_2$bpy) and Pt(bph)(4,4'-(COOC$_2$H$_5$)$_2$bpy) as well as Pt(bph)(bpy)[8] form dimers stacked along the axis perpendicular to the approximate plane of the complex and passing through the Pt atom, whereas the dimers of Pt(bph)(Me$_2$bpy) are in parallel displaced configuration with only the Me$_2$bpy moieties stacked (see Supporting Information, cif files). In the dimers, the bpy ligands are stacked together in Pt(bph)(bpy),[1] whereas the (COOC$_2$H$_5$)$_2$bpy ligands are stacked oppositely in Pt(bph)(4,4'-(COOC$_2$H$_5$)$_2$bpy). The latter stacking mode is similar to that of the Pt(bph)(CO)$_2$ complex we reported previously.[8,9]

Table 3. Selected Bond Lengths (Å), Bond Angles (°) and Torsion Angles (°) Measured Using XRD Crystallography.

Measured	Pt(bph)(4,4'-Me$_2$bpy)	Pt(bph)(bpy)	Pt(bph)(4,4'-Br$_2$bpy)	Pt(bph)(4,4'-(COOC$_2$H$_5$)$_2$bpy)
		Bond length		
Pt – C1	2.006(8)	1.993 (9)	1.994(7)	2.009(4)
Pt – C2	2.016(9)	2.021(10)	2.006(7)	2.002(4)
Pt – N1	2.125(6)	2.101(8)	2.112(5)	2.118(3)
Pt – N2	2.113(6)	2.125(8)	2.128(4)	2.129(3)

		Bond angle		
C1 – Pt – C2	80.6(3)	80.2(4)	81.0(3)	80.5(3)
N1 – Pt – N2	77.3(2)	76.6(3)	77.5(2)	77.4(1)
C1 – Pt – N1	102.3(3)	102.5(3)	102.3(2)	102.3(1)
C2 – Pt – N2	102.8(3)	104.1(3)	103.0(2)	102.7(1)
		Torsion angle		
C-C-N-N	153.82	151.95	150.20	153.84
bph-bpy	28.2	31.3	37.5	32.6

Geometry Optimization Geometry optimization of isolated complexes in acetonitrile solvent conducted using the B3PBE functional gave rise to the largely distorted from planarity X-configurations, as highlighted in the side views shown in Figure 2. In these optimized geometries, the bph-bpy torsion angles were ~5-6° larger than in the XRD results, due to the absence of intermolecular and crystal packing interactions. The ethyl groups of the ester ligands are coplanar with the pyridyl moieties. The torsion angle between the phenyl groups and the pyridyl moieties is 34°. Selected optimized bond lengths, angles and charges were listed in Table 4. The optimized Pt-C bond lengths were in excellent agreement with the XRD measurements, whereas the Pt-N bonds were systematically overestimated, as noted for other Pt(II)[1] and Ru(II) diimine complexes[16,59] and discussed above. The optimized Pt-N bonds were longer than the Pt-C bonds by ~0.13-0.14 Å. The ligand bite angels were in excellent agreement with the XRD results. The Mulliken atomic charges on the Pt atoms increased from left to right along Table 4, as the electron-withdrawing strength of the 2,2'-bipyridine ligand substituents was increased. The geometries of these complexes optimized in gas phase are in agreement with those in acetonitrile solvent. The most notable difference is in the bpy-bph torsion angle that is up to 1.5° larger in gas phase.

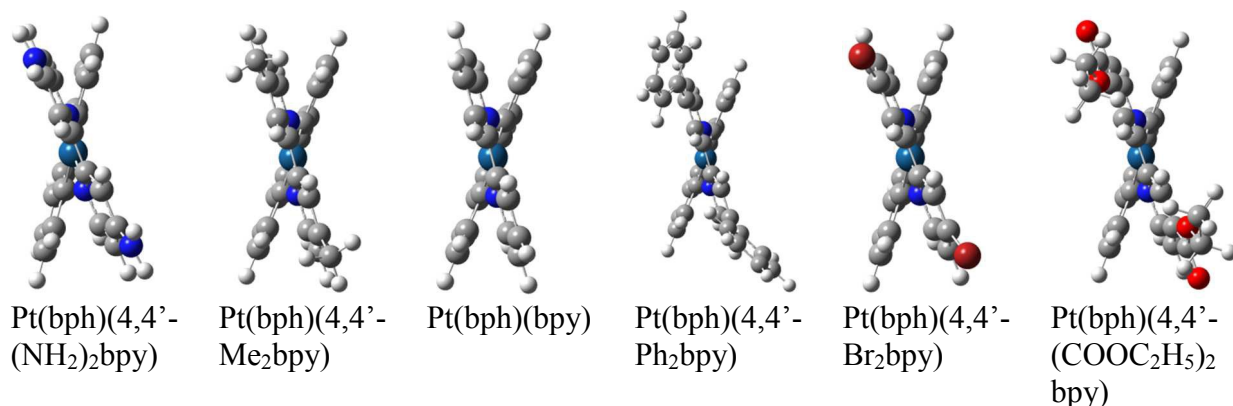| Pt(bph)(4,4'-(NH$_2$)$_2$bpy) | Pt(bph)(4,4'-Me$_2$bpy) | Pt(bph)(bpy) | Pt(bph)(4,4'-Ph$_2$bpy) | Pt(bph)(4,4'-Br$_2$bpy) | Pt(bph)(4,4'-(COOC$_2$H$_5$)$_2$ bpy) |

Figure 2. Geometries of the Complexes Optimized Using the B3PBE/TZVP-QZV-P/CPCM Method Highlighting the bph-bpy Torsion Angle Characteristic of the X-configuration.

Table 4. Platinum-ligand Bond Lengths (Å), Ligand Bite Angles (°) and bph-bpy Torsion Angles (°) optimized for Isolated Complexes in Singlet Ground State (SGS) and Lowest-lying Triplet State (LLTS) in Acetonitrile Solvent Using the B3PBE/TZVP-QZV-P/CPCM Method. The Mulliken atomic charges (|e|) of the Pt atoms and bpy and bph ligand moieties are listed as q (Pt), q (bpy) and q (bph), respectively.

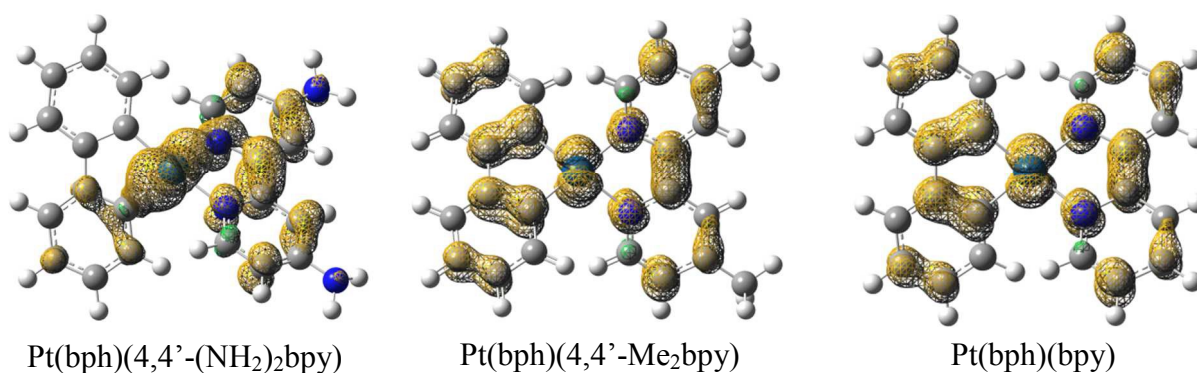| Optimized	Pt(bph)(4,4'-(NH$_2$)$_2$bpy)	Pt(bph)(4,4'-Me$_2$bpy)	Pt(bph)(bpy)	Pt(bph)(4,4'-Ph$_2$bpy)	Pt(bph)(4,4'-Br$_2$bpy)	Pt(bph)(4,4'-(COOC$_2$H$_5$)$_2$bpy)
			SGS			
Pt-C	2.004	2.005	2.006	2.004	2.005	2.005
Pt-N	2.145	2.142	2.141	2.139	2.145	2.135
C-Pt-C	80.5	80.5	80.5	80.5	80.5	80.5
N-Pt-N	76.0	76.2	76.4	76.4	76.2	76.6
bph-bpy	37.3	37.7	36.1	37.3	37.3	38.2
q (Pt)	0.56	0.60	0.60	0.62	0.62	0.65
q (bpy)	0.47	0.41	0.39	0.39	0.36	0.33
q (bph)	-1.03	-1.01	-0.99	-1.01	-0.98	-0.99
			LLTS			
Pt-C	2.004, 2.018	1.975	1.975	1.975	1.973	1.973
Pt-N	2.108, 2.070	2.105	2.108	2.111	2.117	2.118
C-Pt-C	80.8	81.3	81.2	81.2	81.3	81.2
N-Pt-N	78.0	77.9	78.0	77.6	77.7	77.5
bph-bpy	45.3	31.0	31.2	31.0	31.1	31.8
q (Pt)	1.10	0.86	0.84	0.85	0.86	0.86
q (bpy)	-0.13	-0.26	-0.28	-0.29	-0.33	-0.35
q (bph)	-0.97	-0.60	-0.56	-0.56	-0.53	-0.51

The optimized geometries of the LLTS also have X-configurations with bph-bpy torsion angles ~6° shorter than in the SGS, except the Pt(bph)(4,4'-(NH$_2$)$_2$bpy) that undergoes an

extensive distortion to a bph-bpy angle of 45° (Table 4). In the LLTS, the Pt-N and Pt-C bonds are shorter by ~0.03-0.04 Å than those in the respective SGS, except the Pt(bph)(4,4'-(NH₂)₂bpy) complex. In the latter, one of the Pt-N bonds is shorter than the other by ~0.04 Å, which shows this geometry is the only one in the series that deviates from pseudo C_2 symmetry. We also optimized the geometry of the triplet T_1 state of the Pt(bph)(4,4'-(NH₂)₂bpy) complex by constraining it to the C_2 point group and found that the energy of this symmetrical state is 0.12 eV higher than the broken-symmetry LLTS, the latter effectively being the T_0 state. In the T_1 state, the Pt-C and Pt-N bond lengths are 1.981 Å and 2.104 Å, respectively. The bph-bpy torsion is 30.8°. Considering the values for the T_1 state of Pt(bph)(4,4'-(NH₂)₂bpy) and the LLTS of the rest of the complexes, the Pt-N bond lengths increase and the Pt-C bond lengths decrease as the electron-donating strength of the functional group is increased.

The Mulliken atomic charges show that in the SGS to LLTS transition electron density is transferred from the biphenyl ligand and Pt to the bipyridine ligand. Thus, electron-withdrawing groups that facilitate the acceptance of electron density stabilize the LLTS, as manifested in the decreasing LLTS energy (Table 5). Moreover, the electron-donating amine groups destabilize the triplet state and yields a broken symmetry LLTS. The charge on Pt in the LLTS are higher by ~0.2 |e| than those in the SGS and do not correlate well with the electron-withdrawing substituent trends, in particular, as the complex inclosing the strongest electron-donating group (NH₂) has the largest positive charge on the Pt atom. For Pt(bph)(4,4'-(NH₂)₂bpy), the Pt atom charge in the LLTS is higher by 0.54 |e| than that in the respective SGS due to a very extensive charge transfer from Pt to the bpy ligand as a result of the breaking of the pseudo C_2 symmetry. In the T_1 state of Pt(bph)(4,4'-(NH₂)₂bpy), the charges on Pt, bpy and bph are 0.85 |e|, -0.21 |e| and -0.64 |e|, respectively. Considering the latter T_1 state and the LLTS of the rest of the complexes,

the 2,2'-bipyridine ligand charges become less negative and the biphenyl ligand charges become more negative, as the electron-donating strength of the functional group is increased. This is correlated with the bonding of NH_2 groups with the bpy moiety and the character of the LLTS, as discussed below.

The electronic character of the LLTS is assigned based on the spin density distributions[37] presented in Figure 3. The spin densities are localized mainly on the Pt(bph)(bpy), away from the electron-withdrawing and donating substituents. In all complexes except Pt(bph)(4,4'-$(NH_2)_2$bpy), the spin density is evenly distributed over the entire Pt(bph)(bpy) moieties. In the Pt(bph)(4,4'-$(NH_2)_2$bpy) complex, the spin density is localized mostly on the Pt atom and the 2,2-bipyridine ligand. This Pt-localized LLTS is distinct from the rest of the complexes studied and could be a cause for the distinct emission spectrum of Pt(bph)(4,4'-$(NH_2)_2$bpy). The spin density of the T_1 state of the Pt(bph)(4,4'-$(NH_2)_2$bpy) shown in Supporting Information Figure S2 is analogous to those of the LLTS of the rest of the complexes.
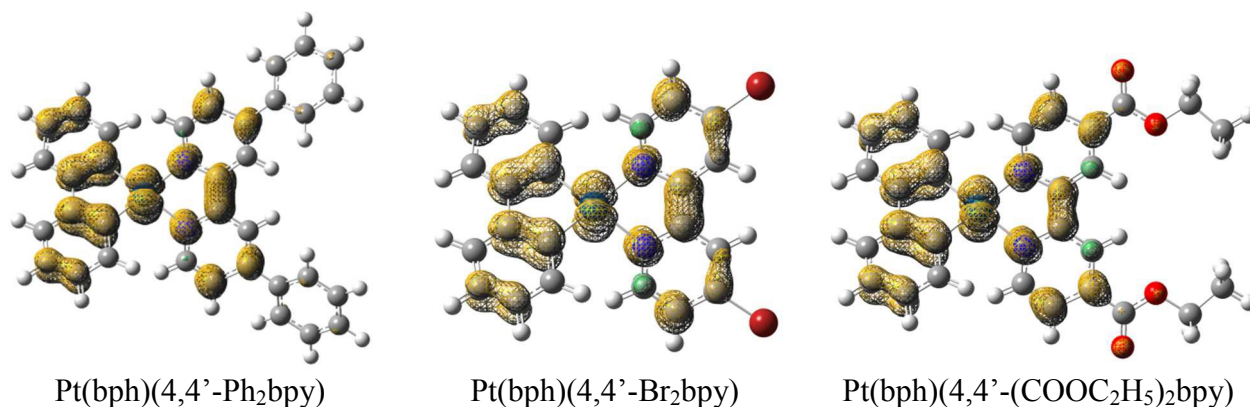

Pt(bph)(4,4'-$(NH_2)_2$bpy)   Pt(bph)(4,4'-Me_2bpy)   Pt(bph)(bpy)

Pt(bph)(4,4'-Ph$_2$bpy)   Pt(bph)(4,4'-Br$_2$bpy)   Pt(bph)(4,4'-(COOC$_2$H$_5$)$_2$bpy)

Figure 3. Electron Spin Density Distributions Around the Complexes Plotted at Isovalue of 0.003 e/Å^3 for the LLTS of Isolated Molecules in Acetonitrile Solvent Computed Using the B3PBE/TZVP-QZV-P/CPCM Method. The α and β spin densities are shown as tan and green meshes, respectively. The percent contributions of major moieties are listed in Table 3.

In Table 5, we list the energies and assignments of the LLTS that according to Kasha's rule[20] would be the emitting states. The LLTS energies decrease in the order from electron-donating to electron-withdrawing substituents in the 2,2'-bipyridine ligand. For all complexes, there is substantial spin density ρ_s on the Pt atom and the ρ_s on the 2,2'-bipyridine ligand is larger than on the biphenyl ligand. The spin density of Pt(bph)(4,4'-(NH$_2$)$_2$bpy) in the LLTS is distributed differently from the rest, as the ρ_s on the Pt atom is about twice as large as that in the rest of the complexes and the ρ_s on the (NH$_2$)$_2$bpy moiety is increased, all to the account of the biphenyl ligand. Thus, only the LLTS of Pt(bph)(4,4'-(NH$_2$)$_2$bpy) is assigned as ^{3}MLCT, whereas the rest are predominantly ^{3}LC$_{bpy-bph}$ with significant ^{3}MLCT character. In the T$_1$ state of Pt(bph)(4,4'-(NH$_2$)$_2$bpy), the spin densities on Pt, bpy and bph are 0.36 |e|, 0.99 |e| and 0.65 |e|, respectively. Considering this T$_1$ state and the LLTS of the rest of the complexes, the Pt atom spin densities increase as the electron-donating strength of the functional group is increased.

Table 5. Lowest-lying Triplet States (LLTS) (in eV and in parentheses in nm) of Isolated Molecules Fully Optimized in Acetonitrile Solvent Using the TD-DFT/B3PBE/TZVP-QZV-P/CPCM Method. The LLTS type is assigned based on the distribution of the 2 unpaired

electrons, labeled as spin densities (ρ_s, in $|e|$) among the Pt atom and the bpy and bph ligand moieties. The spin density distributions are presented in Figure 3.

Complex	LLTS	Type	ρ_s (Pt)	ρ_s (bpy)	ρ_s (bph)
Pt(bph)(4,4'-(NH$_2$)$_2$bpy)	2.12 (584)	^{3}MLCT	0.61	1.12	0.19
Pt(bph)(4,4'-Me$_2$bpy)	1.99 (624)	^{3}LC$_{bpy-bph}$/^{3}MLCT	0.34	0.94	0.72
Pt(bph)(bpy)	1.93 (642)	^{3}LC$_{bpy-bph}$/^{3}MLCT	0.33	0.94	0.74
Pt(bph)(4,4'-Ph$_2$bpy)	1.88 (660)	^{3}LC$_{bpy-bph}$/^{3}MLCT	0.32	0.94	0.74
Pt(bph)(4.4'-Br$_2$bpy)	1.74 (712)	^{3}LC$_{bpy-bph}$/^{3}MLCT	0.31	0.96	0.74
Pt(bph)(4,4'-(COOC$_2$H$_5$)$_2$bpy)	1.57 (788)	^{3}LC$_{bpy-bph}$/^{3}MLCT	0.30	0.94	0.76

Singlet excited electronic states

Singlet excited states (SES) of the complexes were calculated relative to the SGS using the TD-DFT method in acetonitrile solvent. In Table 6, we listed the SES with oscillator strength higher than 0.09 along with assignments of the major contributing electronic transitions. The assignments were made based on the molecular orbital spatial distributions presented in the Supporting Information Figure S3. The normalized percent contributions of the major electronic transitions contributing to the SES were given in parentheses. The lowest-energy SES were found to be associated with the ^{1}MLLCT transition. Higher-lying excited states had large contributions from $\pi \rightarrow \pi^*$ transitions involving biphenyl and bipyridine ligands. Ligand-centered transitions from the phenyl substituent to the bipyridine moiety were noted for the Pt(bph)(4,4'-Ph$_2$bpy) complex due to the close electronic coupling of these aromatic groups in the ligand.

Table 6. Singlet Excited States (SES) (in eV and in parentheses in nm) with Oscillator Strength (f) Higher Than 0.09 of Isolated Molecules in Acetonitrile Solvent Calculated as Vertical Electronic Transitions Using the TD-DFT/B3PBE/TZVP-QZV-P/CPCM Method. The transition types are assigned based on the major contributing electronic transitions with percentages listed in parentheses. The spatial distributions of the molecular orbitals participating in these transitions are shown in Supporting Information Figure S3. MLCT = metal-to-ligand charge transfer; LC= ligand-centered; MLLCT = metal-and-ligand-1-to-ligand-2 charge transfer (see subscripts for ligand 1 and ligand 2); Subscripts denote the major contributing moiety.

Complex	SES	f	Type	Transition
Pt(bph)(4,4'-(NH$_2$)$_2$bpy)	3.04 (408)	0.19	ML$_{bph}$L$_{bpy}$CT	H-1→L (100%)
	3.82 (324)	0.16	L$_{bph}$L$_{bpy}$CT, π→π*$_{bph}$	H-1→L+1 (90%)
	4.42 (280)	0.10	ML$_{bpy}$CT, ML$_{bph}$CT	H-2→L+1 (77%)
	4.66 (266)	0.23	ML$_{bph}$L$_{bpy}$CT	H-9→L (30%)
			L$_{bph}$MCT, d→d	H→L+7 (32%)
	4.69 (264)	0.11	π→π*$_{bpy}$, ML$_{bpy}$CT	H-9→L (30%)
			ML$_{bpy}$CT	H→L+7 (32%)
	4.73 (262)	0.18	ML$_{bpy}$CT	H-2→L+3 (44%)
			π→π*$_{bph}$, d→d	H→L+6 (28%)
Pt(bph)(4,4'-Me$_2$bpy)	2.92 (425)	0.21	ML$_{bph}$L$_{bpy}$CT	H-1→L (100%)
	3.77 (329)	0.10	ML$_{bpy}$CT	H-2→L (100%)
	4.43 (280)	0.49	π→π*$_{bpy}$, ML$_{bpy}$CT	H-6→L (72%)
	4.66 (266)	0.11	ML$_{bpy}$CT	H-4→L+1 (45%)
			ML$_{bph}$L$_{bpy}$CT	H-9→L (31%)
	4.80 (258)	0.25	ML$_{bph}$L$_{bpy}$CT	H-3→L+2 (42%)
			ML$_{bph}$CT	H-2→L+3 (44%)
Pt(bph)(bpy)	2.84 (436)	0.19	π→π*$_{bpy}$	H-6→L (100%)
	4.37 (284)	0.45	ML$_{bph}$L$_{bpy}$CT	H-7→L (75%)
	4.80 (258)	0.34	π→π*$_{bph}$, ML$_{bph}$L$_{bpy}$CT	H-3→L+3 (60%)
	5.07 (244)	0.10	ML$_{bph}$L$_{bpy}$CT, π→π*$_{bph}$	H-4→L+3 (86%)
	5.27 (235)	0.12	π→π*$_{bph}$, d$_{xz}$→d$_{yz}$	H-1→L+7 (39%)
			π→π*$_{bpy}$	H-6→L+2 (20%)
	5.58 (222)	0.20	π→π*$_{bph}$, d$_{xz}$→d$_{yz}$	H-1→L+6 (96%)
Pt(bph)(4,4'-Ph$_2$bpy)	2.75 (451)	0.29	ML$_{bph}$L$_{bpy}$CT	H-1→L (97%)
	3.98 (311)	0.14	LC$_{Ph→bpy}$, d→d	H-6→L (50%)
			ML$_{bph}$L$_{bpy}$C	H-3→L+2 (33%)
	4.03 (308)	0.17	ML$_{bph}$L$_{bpy}$CT	H-3→L+2 (63%)
			LC$_{Ph→bpy}$, d→d	H-6→L (31%)
	4.07 (305)	0.11	LC$_{Ph→bpy}$	H-5→L (91%)
	4.17 (297)	0.11	LC$_{bph, Ph→bpy}$	H-7→L (41%)
			π→π*$_{bph}$	H-1→L+3 (31%)
	4.39 (282)	0.13	ML$_{bph}$L$_{bpy}$CT	H-4→L+1 (97%)
	4.46 (278)	0.13	ML$_{bph}$L$_{bpy}$CT	H-4→L+2 (91%)
	4.67 (265)	0.12	π→π*$_{bpy}$	H-5→L+1 (43%)
			ML$_{bph-Ph}$CT	H-2→L+6 (22%)
	4.77 (260)	0.16	ML$_{bph-Ph}$CT	H-2→L+6 (50%)
			π→π*$_{bpy}$	H-5→L+1 (13%)
	4.78 (260)	0.21	π→π*$_{bpy}$	H-5→L+1 (24%)
			π→π*$_{bph}$, d→d	H-3→L+3 (15%)

	4.79 (258)	0.26	$LC_{Ph \to bpy}$	H-5→L+2 (33%)
			$LC_{Ph \to bpy}$	H-5→L+1 (16%)
	4.87 (256)	0.13	$ML_{bpy}CT, \pi \to \pi^*_{bpy}$	H-6→L+2 (67%)
	5.52 (224)	0.17	$ML_{bph}L_{bpy}CT, \pi \to \pi^*_{bph}$	H-1→L+9 (63%)
	5.59 (221)	0.12	$LC_{bpy \to bph}$	H-5→L+3 (29%)
			$ML_{bph}L_{bpy}CT$	H→L+10 (12%)
$Pt(bph)(4.4'-Br_2bpy)$	2.67 (464)	0.21	$ML_{bph}L_{bpy}CT$	H-1→L (100%)
	3.50 (354)	0.10	$ML_{bph}L_{bpy}CT$	H-1→L+1 (100%)
	4.32 (287)	0.13	$ML_{bph}L_{bpy}CT$	H-4→L+1 (54%)
			$\pi \to \pi^*_{bpy}$	H-7→L (33%)
	4.44 (279)	0.36	$ML_{bph}L_{bpy}CT$	H-4→L+1 (43%)
			$\pi \to \pi^*_{bpy}, d_{yz} \to d_{xz}$	H-7→L (35%)
	4.73 (262)	0.20	$\pi \to \pi^*_{bph}, d \to d$	H-3→L+3 (32%)
			$ML_{bph}L_{bpy}CT$	H→L+9 (32%)
	4.81 (258)	0.19	$\pi \to \pi^*_{bph}, d \to d$	H-3→L+3 (38%)
			$ML_{bph}CT$	H-2→L+6 (29%)
$Pt(bph)(4,4'-(COOC_2H_5)_2bpy)$	2.51 (493)	0.14	$ML_{bph}L_{bpy}CT$	H-1→L (70%)
	2.67 (464)	0.18	$ML_{bph}L_{bpy}CT$	H→L+1 (70%)
	4.02 (308)	0.26	$\pi \to \pi^*_{bpy}, d_{yz} \to d_{xz}$	H-7→L (84%)
	4.69 (265)	0.14	$\pi \to \pi^*_{bph}, d \to d$	H-3→L+3 (36%)
			$ML_{bph}L_{bpy}CT$	H-1→L+4 (43%)
	4.82 (257)	0.26	$\pi \to \pi^*_{bph}, d \to d$	H-3→L+3 (45%)
			$ML_{bph}L_{bpy}CT$	H-1→L+4 (23%)

The spatial distributions of the HOMO, HOMO-1, and LUMO of the complexes are presented in Figure 4. The HOMO and HOMO-1 are localized on the biphenyl ligand and Pt moieties, and the LUMO was localized on the bipyridine ligand. These results confirm that spatial distributions of the HOMO and HOMO-1 were similar. The localization of the LUMOs on electron-donating and electron-withdrawing substituents is insignificant. The electronic transition from HOMO-1 to LUMO is found to be the main contributor to the [1]MLLCT states associated with the lowest-energy band we observed in the absorption spectra of the complexes.

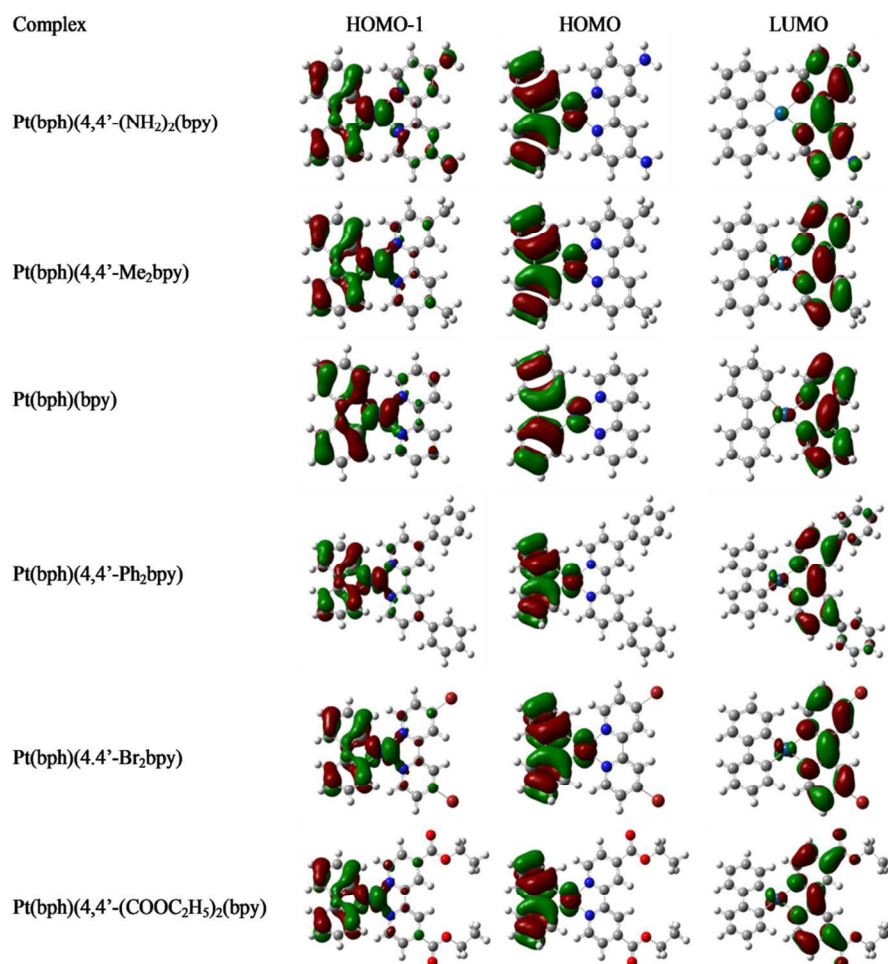| Complex	HOMO-1	HOMO	LUMO
Pt(bph)(4,4'-(NH₂)₂(bpy)			
Pt(bph)(4,4'-Me₂bpy)			
Pt(bph)(bpy)			
Pt(bph)(4,4'-Ph₂bpy)			
Pt(bph)(4.4'-Br₂bpy)			
Pt(bph)(4,4'-(COOC₂H₅)₂(bpy)			

Figure 4. Spatial Distributions of the HOMO, HOMO-1, and LUMO of the Complexes Plotted at an Isovalue of 0.03 au for the SGS of Isolated Molecules in Acetonitrile Solvent Computed Using the B3PBE/TZVP-QZV-P/CPCM Method. The percent contributions of major transitions are listed in Table 6. Red and green isosurface colors denote + and – nodes, respectively.

UV/Visible Absorption and Emission Spectra

The lowest-energy bands of the experimental adsorption spectra of the complexes are presented in Figure 5a.   These bands, attributed to the characteristic MLCT transition, undergo bathochromic and hypsochromic shifts relative to the parent Pt(bph)(bpy) complex in the presence of electron-withdrawing and electron-donating substituents, respectively. The emission spectra, presented in Figure 5b, are broad with discernible vibronic coupling of approximately ~1156 – 1173 cm^{-1} as reported earlier for Pt(bph)(bpy).[1] The emission spectrum of Pt(bph)(4,4'-

(NH$_2$)$_2$bpy) is distinct from the rest, as presented in Supporting Information Figure S4. Excitation spectra were also collected and corresponded to the absorption profiles.
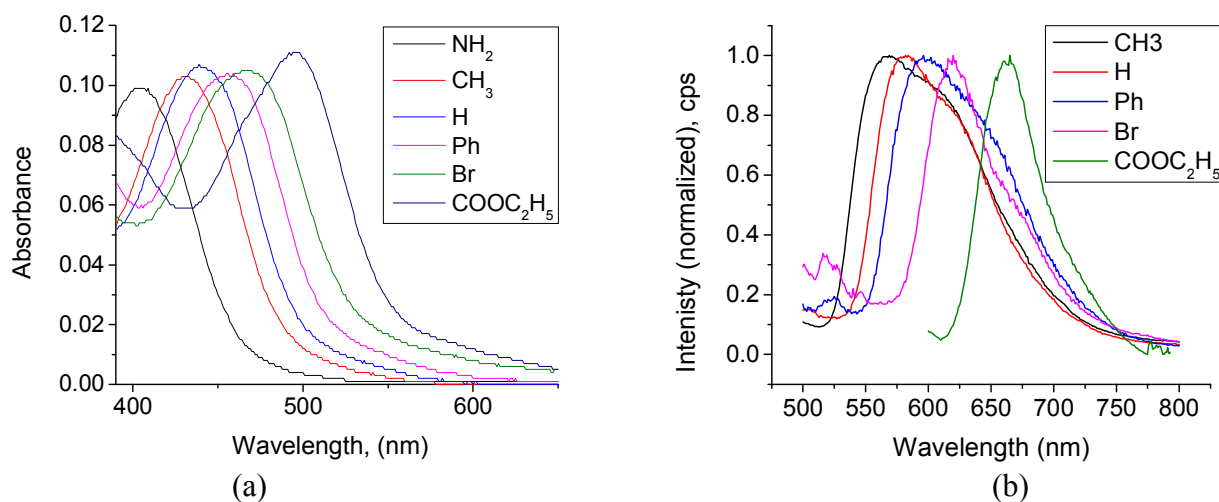

(a)

(b)

Figure 5. Experimental Absorption (a) and Emission spectra (b) of Pt(bph)(4,4'-X$_2$bpy). Spectra were obtained in butyronitrile at room temperature for absorption and at 77 K for emission.

Experimental values of the major absorption peak maxima and molar extinction coefficients (in parentheses) for the complexes are listed in Table 7 along with calculated SES energies (from Table 6). Experimental emission peak maxima and emission lifetimes for the complexes in a butyronitrile glass 77 K are also presented in Table 7 along with calculated LLTS energies and assignments. The largest emission lifetime of 2.25 μs is measured for Pt(bph)(4,4'-(NH$_2$)$_2$bpy) that features a distinctly more structured emission spectrum compared to the rest of the series. The calculated and experimental results are in a very good agreement.

Table 7. Experimental and Calculated Electronic Absorption and Emission Results. MLCT = metal-to-ligand charge transfer; LC= ligand-centered; MLLCT = metal-and-ligand-1-to-ligand-2 charge transfer. Subscripts denote the major contributing moiety.

Complex	$\lambda_{abs}{}^a$ (ε, M^{-1}cm^{-1})	$\lambda_{SES},{}^b$	Type$_{SES}$	$\lambda_{em}{}^c$, nm (77K)^d	τ, μs (77K)^d	$\lambda_{LLTS},{}^e$ nm	Type$_{LLTS}$
Pt(bph)(4,4'-(NH$_2$)$_2$bpy)	257 (2.8 x 10^4)	262, 264, 266	$\pi\rightarrow\pi^*_{bpy}$	503	2.25	584	^{3}MLCT
	323 (5.9 x 10^3)	324	MLLCT				
	405 (3.6 x 10^3)	408	MLLCT				
Pt(bph)(4,4'-Me$_2$bpy)	259 (2.9 x 10^4)	258	MLLCT	566	0.83	624	^{3}LC, ^{3}MLCT
	286 (1.9 x 10^4)	280	$\pi\rightarrow\pi^*_{bpy}$				
	304 (1.5 x 10^4)	329	MLCT				
	420 (6.1 x 10^3)	425	MLLCT				
Pt(bph)(bpy)	226 (2.7x10^4)	222	$\pi\rightarrow\pi^*_{bph}$	584	0.69	642	^{3}LC, ^{3}MLCT
	258 (2.6x10^4)	258	$\pi\rightarrow\pi^*_{bph}$				
	289 (1.7 x 10^4)	284	$\pi\rightarrow\pi^*_{bph}$				
	440 (5.6x 10^3)	436	MLCT				
Pt(bph)(4,4'-Ph$_2$bpy)	221 (2.1 x 10^4)	221, 224	$\pi\rightarrow\pi^*_{bph}$	600	1.00	660	^{3}LC, ^{3}MLCT
	252 (2.6 x 10^4)	256	$\pi\rightarrow\pi^*_{bph}$				
	264 (2.4 x 10^4)	259, 260	$\pi\rightarrow\pi^*_{bph}$				
	456 (4.6 x 10^3)	451	MLCT				
Pt(bph)(4,4'-Br$_2$bpy)	294 (2.0 x 10^4)	279, 287	$\pi\rightarrow\pi^*_{bph}$	620	0.37	712	^{3}LC, ^{3}MLCT
	340 (1.0 x 10^4)	354	$\pi\rightarrow\pi^*_{bph}$				
	470 (6.0 x 10^3)	464	MLCT				
Pt(bph)(4,4'-(COOC$_2$H$_5$)$_2$bpy)	252 (3.2 x 10^4)	257	$\pi\rightarrow\pi^*_{bph}$	670	0.17	788	^{3}LC, ^{3}MLCT
	320 (1.9 x 10^4)	308	$\pi\rightarrow\pi^*_{bph}$				
	500 (8.2 x 10^3)	493	MLCT				

^{a} in acetonitrile (experiment)
^{b} in acetonitrile (TD-DFT)
^{c} λ_{ex} at MLCT maxima
^{d} in butyronitrile (experiment)
^{e} in acetonitrile (DFT)

Electrochemistry

Table 8 lists the half-wave reduction potentials E$_{1/2red}$ determined for the complexes over the range of 0.0 V to -2.0 V vs. the AgNO$_3$ reference electrode. Within this range, Δ_{EP}, where Δ_{EP} is the difference between the reduction and oxidation peak of the redox active couple determined by cyclic voltammetry, varied from 75 to 100 mV consistent with other reports found for one

electron transfer processes in non-aqueous solvents.[72]   Irreversible electrochemical behavior was

found in the range of 0 V to +2.0 V vs. the AgNO$_3$ reference electrode for the compounds and

was not examined further. The solubility of Pt(bph)(4,4'-(NH$_2$)$_2$bpy) in dichloromethane was too

low to study its electrochemical behavior.   Figure 6 presents the differential pulse

voltammograms of the complexes. The E$_{1/2red}$ values and voltammograms shift to lower and

higher voltages relative to Pt(bph)(bpy) in the presence of electron-withdrawing and electron-

donating substituents, respectively, following the trends of the absorption and emission spectra.

Table 8. Electrochemical Reduction Potentials E$_{1/2}$ of Pt(bph)(4,4'-X$_2$bpy).

Complex	E$_{1/2red}$(V)^a
Pt(bph)(4,4'-(NH$_2$)$_2$bpy)	NA^b
Pt(bph)(4,4'-Me$_2$bpy)	-1.500
Pt(bph)(bpy)	-1.410
Pt(bph)(4,4'-Ph$_2$bpy)	-1.316
Pt(bph)(4,4'-Br$_2$bpy)	-1.209
Pt(bph)(4,4'-(COOC$_2$H$_5$)$_2$bpy)	-1.010

a: 0.1 M TBAH in dichloromethane
b: Not available due to low solubility in dichloromethane
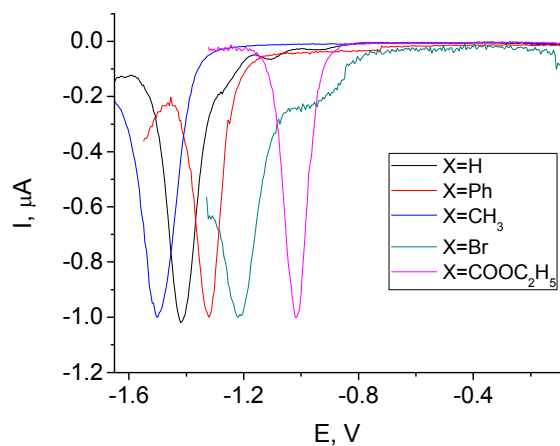

Figure 6. Differential Pulse Voltammograms of Pt(bph)(4,4'-X$_2$bpy).

Discussion

Structures

As noted from the results in Table 3, bond distances and bond angles from XRD in solid state show little dependence on substituent electron-donating and electron-withdrawal effects. However, these substituent effects are evident in the ^{1}H NMR spectra of the complexes. For Pt(bph)(4,4'-(NH$_2$)$_2$bpy), the bipyridyl ^{1}H chemical shifts appear mostly upfield at 7.24-8.68 ppm, while those of Pt(bph)(4,4'-(COOC$_2$H$_5$)$_2$bpy) are found downfield at 7.83-9.40 ppm.

It is important to examine the effect of substituents on bonding within the bipyridine ligand. The Mayer bond order between the N of the amine group and the C atom bonded to it was calculated to be 1.25 in the ground state of the complex and 1.18 in the LLTS, indicating a stronger bonding (exhibited as a partial double bond) compared to that in methylamine with a C-N bond order of 0.95 in singlet and 0.99 in the LLTS. Such extended conjugation of the bipyridine ligand π-system is not obtained in other complexes. For example, in Pt(bph)(4,4'-(COOC$_2$H$_5$)$_2$bpy) the Mayer bond order of the C-C bond at the substitution site of bipyridine was calculated to be 0.96 in the ground state and 0.98 in the LLTS. Also, in Pt(bph)(4,4'-Ph$_2$bpy) the Mayer bond order of the C-C bond at the substitution site was calculated as 0.88 for both the singlet ground and lowest-lying triplet states.

Free Energy Correlations

In order to assess the effects of substituents on properties of the complexes in the series, linear correlations between experimental and computational results are examined with respect to Hammett sigma constants, σ, and in some cases with respect to each other. For consistency, only di-substituents that are para- with respect to the bipyridyl N atoms have been investigated (σ_p).

Absorption and Emission The correlations of experimental lowest-energy transition and calculated ^{1}MLLCT SES (singlet excited states) for the complexes with σ_p presented in Figure 7(a) highlight the impressive agreement between theory and experiment. The energy of lowest-lying electronic transitions determined from both experiment and calculation increases in the order Pt(bph)(4,4'-(COOC$_2$H$_5$)$_2$bpy) < Pt(bph)(4,4'-Br$_2$bpy) < Pt(bph)(4,4'-Ph$_2$bpy) < Pt(bph)(bpy) < Pt(bph)(4,4'-Me$_2$bpy) < Pt(bph)(4,4'-(NH$_2$)$_2$bpy). The linear fitting results listed in Supporting Information Table S3 indicate that experiment and theory substantiate each other.
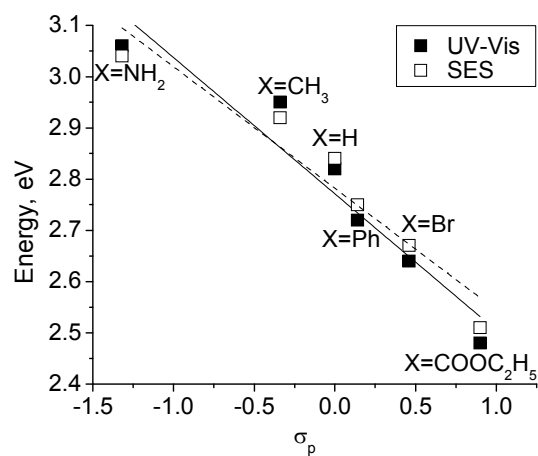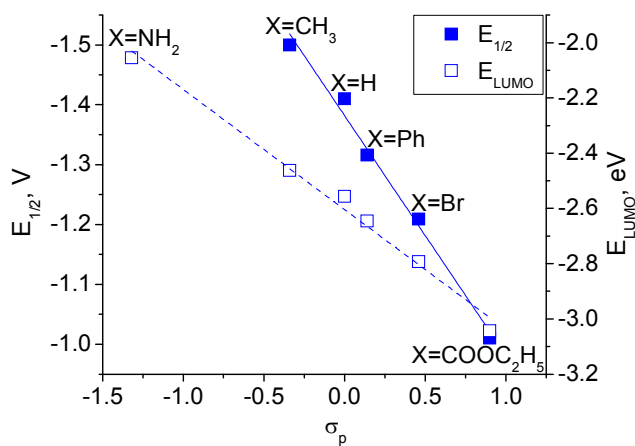

(a)
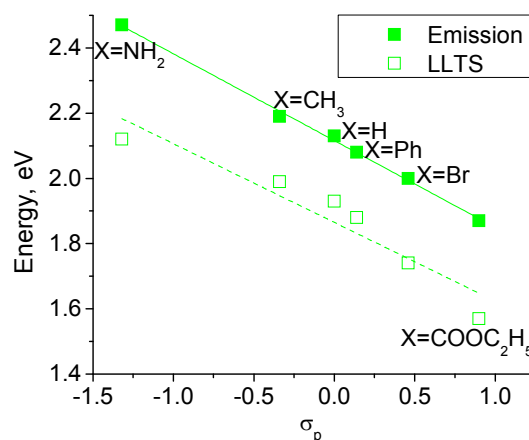
(b)
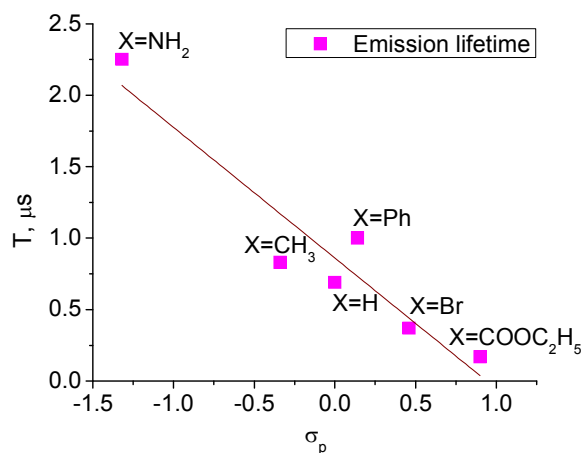
(c)

(d)

Figure 7. Experimental UV-Vis Absorption and Calculated [1]MLLCT State Energies *vs* σ_p (a), Experimental Emission and Calculated LLTS Energies *vs* σ_p (b), Experimental Emission Lifetime *vs* σ_p (c), and Electrochemical Reduction Potential $E_{1/2red}$ and E_{LUMO} *vs* σ_p (d) for the Pt(bph)(4,4'-X_2bpy) Complexes. The linear fitting analysis results are listed in Supporting Information Table S3.

The correlations of the experimental emission and calculated LLTS energies with σ_p are presented in Figure 7(b). These results show that the LLTS energies are systematically lower than the emission energies by 0.2 eV, which falls within the underestimation of 0.25 eV reported in the literature.[37,43] The linear fitting analysis results for absorption and emission (Figures 7(a) and 7(b)) yield slopes in the relatively narrow range from -0.22 to -0.27. The intercepts for experimental emission and LLTS are lower than those for adsorption by 0.7 eV and 0.9 eV, respectively, representing estimates of the sum of the non-radiative relaxation energies for internal conversion and intersystem crossing. The emission lifetimes also correlate linearly with the Hammett constant, as shown in Figure 7(c), in agreement with an earlier report for para-substituted tetraphenyl porphyrin carbonyl complexes of ruthenium(II).[73] Complete linear fitting results are available in Supporting Information Table S3. The emission spectrum of Pt(bph)(4,4'-(NH_2)_2bpy) features a shoulder at 584 nm (2.12 eV) and peaks at about 541 nm (2.29 eV) and 503 nm (2.47 eV), as shown in Supporting Information Figure S3. The spacing between the peaks is ~ 1400 cm^{-1} in the range previously attributed to ring breathing modes in transition metal complexes containing bipyridine ligands.[74]

Electrochemistry Linear correlations of the electrochemical reduction potentials $E_{1/2red}$ with σ_p as shown in Figure 7(d) yield an impressive R^2 value of 0.99. Calculated absolute LUMO energies for complexes in acetonitrile solvent are also plotted *vs* σ_p in Figure 7(d) and give an R^2 value of 0.90. Electron-withdrawing substituents make the reduction of the complexes more thermodynamically favorable (have less negative $E_{1/2red}$) and correlate with lower E_{LUMO}. The

opposite dependence holds for the electron-donating methyl substituent. Electron affinity, a more physical descriptor of a reduction potential that unlike the LUMO energy accounts for orbital relaxation, was also examined. The electron affinity, calculated as the total energy of the anion minus the total energy of the neutral complex, was found to correlate linearly with the Hammett σ_p, as shown in Supporting Information Figure S5.

Energy Gap Control The HOMO-LUMO energy gap is a very important electronic structure characteristic of these complexes, as it is related to their photochemical and redox properties. The correlation of the HOMO-LUMO gap calculated using DFT with σ_p presented in Figure 8 indicates that by using electron-withdrawing and electron-donating substituents the properties of Pt(II) diimine complexes can be controlled to a large extent by using functional groups, as demonstrated by the R^2 value of 0.92.
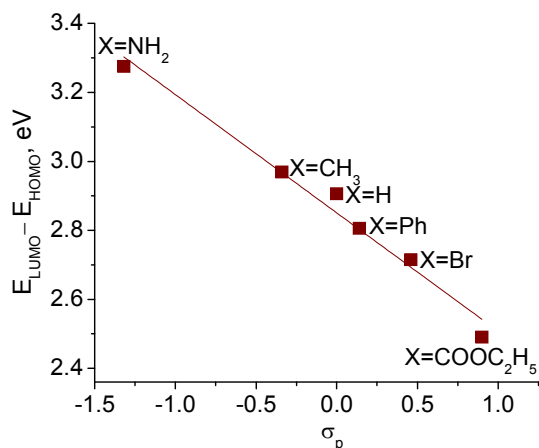
Figure 8. Calculated $E_{LUMO} - E_{HOMO}$ energy gap *vs* σ_p for Pt(bph)(4,4'-X_2bpy). The linear fitting analysis results are listed in Supporting Information Table S3.

    The HOMO-LUMO energy gap calculated using DFT gives a reasonable approximation of the lowest excitation energy without taking into account orbital relaxation.[75] The main source of error in energy gap calculations using DFT is the inaccuracy in the calculation of the LUMO

energy. The TD-DFT calculations yield vertical electronic energies of the SES and allow direct calculation of the HOMO-LUMO gap as the energy of the lowest-lying SES. The correlation of the HOMO-LUMO gap calculated as the lowest-lying SES presented in Supporting Information Figure S6. However, lowest-lying excited states could be forbidden and not observed experimentally. The oscillator strength of an excited state computed using TD-DFT is related with molar absorptivity coefficient and allows identification of the lowest-energy transitions observable experimentally, e.g., using absorption UV-Vis spectroscopy. The ^{1}MLLCT SES listed in Table 6 and correlated with σ_p in Figure 7(a) represents the lowest-lying SES with oscillator strength higher than 0.09 that are observable as the lowest-energy transitions in the absorption spectra.

Predictions for Pt(bph)(4,4'-(X)$_2$bpy, X=CN, NO$_2$ and Me$_2$N These impressive correlations are employed to predict the experimental spectroscopic properties of the complexes Pt(bph)(4,4'-(CN)$_2$bpy), Pt(bph)(4,4'-(NO$_2$)$_2$bpy) and Pt(bph)(4,4'-(Me$_2$N)$_2$bpy) that have not yet been synthesized. The σ_p values for two CN, NO$_2$ and (CH$_3$)$_2$N substituents are 1.32, 1.56 and -1.66 respectively. These σ_p values indicate that the CN and NO$_2$ functional groups are stronger electron-withdrawers than those in the series we explore experimentally, whereas the Me$_2$N is a stronger electron-donor than those in the series. The geometries of these complexes are optimized in the SGS and LLTS, and the singlet excited states are calculated as described above. The results are presented in Supporting Information Tables S4-S6 and Figures S7 and S8. The main distinctions of the complexes containing CN and NO$_2$ from the series of 6 complexes presented above are the larger Pt atom charges in the SGS, lower-lying LLTS, and smaller changes in Pt-C and Pt-N bond lengths in the LLTS compared to SGS. In particular, the energy of the LLTS of Pt(bph)(4,4'-(NO$_2$)$_2$bpy) is about half that of Pt(bph)(4,4'-(NH$_2$)$_2$bpy).

Similar to Pt(bph)(4,4'-(NH$_2$)$_2$bpy), the Pt(bph)(4,4'-(Me$_2$N)$_2$bpy) complex has a broken-symmetry LLTS and a T$_1$ state with C_2 symmetry 0.13 eV above the LLTS, according to our computational studies. Also, the Mulliken charge and spin density distributions in the SGS, LLTS and T$_1$ states of these two complexes are very similar. The Mayer bond orders for the C(bpy)-N(Me$_2$N) bond are 1.33 and 1.29 in the SGS and LLTS, respectively, indicating stronger bonding compared to the respective values of 1.25 and 1.18 for Pt(bph)(4,4'-(NH$_2$)$_2$bpy).

The properties of Pt(bph)(4,4'-(CN)$_2$bpy), Pt(bph)(4,4'-(NO$_2$)$_2$bpy) and Pt(bph)(4,4'-(Me$_2$N)$_2$bpy) are predicted based on the linear fitting analysis results listed in Table S1 and listed in Table 9. The E$_{MLLCT}$, E$_{LLTS}$, E$_{LUMO}$ and energy gap predictions for Pt(bph)(4,4'-(CN)$_2$bpy) compare favorably with the respective calculated values. For the Pt(bph)(4,4'-(NO$_2$)$_2$bpy) complex, the deviations of the predicted values from the respective calculated values are significant. This may be due in part to the strong influence of the nitro group as reported by others for heterocyclic platinum(II) complexes.[76,77] For the Pt(bph)(4,4'-(Me$_2$N)$_2$bpy) complex, the agreement between predicted and actual values is intermediate. These predictions represent extensive extrapolation as the σ_p values of the CN and NO$_2$ groups are significantly larger and those of Me$_2$N are smaller than those of the linear fitting series. Nevertheless, these predictions demonstrate an important approach for preliminary evaluation or *in silico* screening of unknown compounds.

Table 9. Predicted and Actual Properties of Pt(bph)(4,4'-(X)$_2$bpy), X=CN, NO$_2$ and Me$_2$N. The predicted values are calculated from the σ_p values of the CN, NO$_2$ and (CH$_3$)$_2$N groups as well as the slope and intercept values calculated for Figures 7 and 8 and listed in Supporting Information Table S3. The actual values are calculated using the B3PBE/TZVP-QZV-P/CPCM Method.

Complex	$E_{SES\text{-}MLLCT}$	$E_{Abs\text{-}MLLCT}$	E_{LLTS}	E_{Em}	$E_{1/2}$	E_{LUMO}	E gap
			Pt(bph)(4,4'-(CN)$_2$bpy)				
Predicted	2.48	2.41	1.56	1.80	-0.85	-3.19	2.40
Actual	2.53	-	1.41	-	-	-3.30	2.31
			Pt(bph)(4,4'-(NO$_2$)$_2$bpy)				
Predicted	2.42	2.35	1.51	1.75	-0.76	-3.30	2.32
Actual	2.13	-	1.07	-	-	-3.76	1.89
			Pt(bph)(4,4'-(Me$_2$N)$_2$bpy)				
Predicted	3.22	3.16	2.46	2.28	-2.04	-1.87	3.41
Actual	3.03	-	2.17	-	-	-2.00	3.31

Conclusion

Derivatives of Pt(bph)(bpy) with varying electron-withdrawing and donor substituents attached to the 4,4' positions of bipyridine have been synthesized and characterized. The XRD results and geometry optimization using DFT showed that all the complexes in the series have an X-configuration with torsion angles of 28-30° in single crystals and 37° in acetonitrile solution. Molecular orbital diagrams show that the HOMOs have Pt-biphenyl character and the LUMOs are localized on the bipyridyl group. Electron-donating and withdrawing effects were analyzed using Pt atom charge and spin density analyses. The lowest-lying triplet states were also optimized and assigned based on the localization of the electron spin density. The TD-DFT method was employed to predict the singlet excited states in acetonitrile that were found to be in a very good agreement with the electronic absorption spectral peaks in the same solvent.

Correlations of calculated and experimental results with the Hammett constants for para-substitution position were established in order to analyze the electron-withdrawing and donating effects on the coordination sphere of the complexes in the series. The correlations of calculated [1]MLLCT and UV-Vis spectra lowest-energy bands with the Hammett σ_p constants highlighted these charge transfer effects. The calculated LUMO energies as well as measured reduction half-

wave potentials and emission lifetimes were also correlated with σ_p values. Moreover, the experimental emission and calculated LLTS energies indicated that the calculated values are systematically lower that those measured, in agreement with previous reports.

The most important correlation established was between the HOMO-LUMO energy gap, a very important characteristic that determines the applicability of compounds in photo- and electrochemical devices, and the σ_p values for the ligand substituents.   Predictions of spectroscopic and electrochemical properties for three compounds that have not been synthesized are also presented as guidelines for further research effort.   In light-harvesting devices, the energy gap must overlap with the conduction band and the E_{LUMO} must be within or above the conduction band of a semiconductor, such as TiO_2.   Our results demonstrate that by varying the substituents attached to the bipyridyl ring, the HOMO-LUMO gap and LUMO energy can be tuned up.   The correlations and insights presented here could help screen molecular candidates and rationally design improved optoelectronic, photochemical and photocatalytic devices.

Acknowledgments

Research Officer at the National Institute for Nanotechnology and Adjunct Professor at the Department of Mechanical Engineering, University of Alberta, Edmonton, Alberta, Canada.

Supplementary Information: Additional computational and experimental results. This material is available free of charge via the Internet at http://pubs.acs.org

References and Notes:

1 D. P. Rillema, A. J. Cruz, C. Moore, K. Siam, A. Jehan, D. Base, T. Nguyen and W. Huang, *Inorg. Chem.*, 2012, **52**, 596-607.

2 D. P. Rillema, A. J. Cruz, B. J. Tasset, C. Moore, K. Siam and W. Huang, *J. Mol. Struct.*, 2013, **1041**, 82-91.

3 C. Cornioley-Deuschel and A. von Zelewsky, *Inorg.Chem.*, 1987, **26**, 3354-3358.

4 M. Maestri, D. Sandrini, V. Balzani, A. von Zelewsky, C. Cornioley-Deuschel and P. Joliet, *Helv. Chim. Acta*, 1988, **71**, 1053-1059.

5 N. Simhai, C. N. Iverson, B. L. Edelback and W. D. Jones, *Organometallics*, 2001, **20**, 2759-2766.

6 C. B. Blanton, Z. Murtaza, R. J. Shaver and D. P. Rillema, *Inorg. Chem.*, 1992, **31**, 3230-3235.

7 (*a*) M. R. Plutino, L. M. Scolaro, A. Albinati and R. Romeo, *J. Am. Chem. Soc.*, 2004, **126**, 6470-6484; (*b*) M. R. Plutino, L. M. Scolaro, R. Romero and A. Grassi, *Inorg. Chem.*, 2000, **39**, 2712-2720.

8 Y. Chen, J. W. Merkert, Z. Murtaza, C. Woods and D. P. Rillema, *Inorg. Chim. Acta*, 1995, **240**, 41-47.

9 G. Y. Zheng and D. P. Rillema, *Inorg. Chem.*, 1998, **37**, 1392-1397.

10 S. A. Gardner, H. B. Gordon and M. P. Rausch, *Organomet. Chem.*, 1973, **60**, 179-188.

11 Y. Chen, C. Woods, M. W. Perkovic and D. P. Rillema, *J. Chem. Crystallogr.*, 1996, **26**, 527-531.

12 C. B. Blanton and D. P. Rillema, *Inorg. Chim. Acta*, 1990, **168**, 145-147.

13 C. Karakus, L. H. Fischer, S. Schmeding, J. Hummel, N. Risch, M. Schäferling and E. Holder, *Dalton Trans.*, 2012, **41**, 9623−9632.

14 X. Mou, Y. Wu, S. Liu, M. Shi, X. Liu, C. Wang, S. Sun, Q. Zhao, X. Zhou and W. Huang, *J. Mater. Chem.*, 2011, **21**, 13951−13962.

15 (*a*) H. Yersin, T. Fischer, R. Czerwieniec and U. Monkowius, *Int. Appl.* WO2009112152 A1 20090917, 2009. (*b*) H. Yersin, T. Fischer, R. Czerwieniec and U. Monkowius, *Ger. Offen.* DE102008013691 A1 20090917, 2009. (*c*) H. Yersin, U. Monlowius and R. Czerwieniec, *Ger. Offen.* DE102006017485 A1 20071018, 2007**.**

16 S. R. Stoyanov, J. M. Villegas, A. J. Cruz, L. L. Lockyear, J. H. Reibenspies and D. P. Rillema, *J. Chem. Theory Comput.*, 2005, **1**, 95-106.

17 S. R. Stoyanov, J. M. Villegas and D. P. Rillema, *Inorg. Chem.*, 2003, **42**, 7852-7860.

18 J. Kalinowski, V. Fattori, M. Cocchi and J. A. G. Williams, *Coord. Chem. Rev.*, 2011, **255**, 2401−2425.

19 J. A. G. Williams, *Top. Curr. Chem.*, 2007, **281**, 205−268.

20 M. Kasha, *Discuss. Faraday Soc.*, 1950, **9**, 14−19.

21 K. E. Henry, R. G. Balasingham, A. R. Vortherms, J. A. Platts, J. F. Valliant, M. P. Coogan, J. Zubieta and R. P. Doyle, *Chem. Sci.*, 2013, **4**, 2490−2495.

22 Y.-S. Yeh, Y.-M. Cheng, P.-T. Chou, G.-H. Lee, C.-H. Yang, Y. Chi, C.-F. Shu and C.-H. Wang, *ChemPhysChem*, 2006, **7**, 2294−2297.

23 (*a*) P. Hohenberg and W. Kohn, *Phys. Rev.*, 1964, **136**, B864; (*b*) W. Kohn and L. J. Sham, Phys. Rev., 1965, **140**, A1133.

24 C. A. Mitsoupoulou, C. E. Dagas and C. J. Makedonas, *J. Inorg. Biochem.*, 2008, **102**, 77–86.

25 L. Wang, J. Wen, H. He and J. Zhang, *Dalton Trans.*, 2014, **43**, 2849-2858.

26 S. R. Stoyanov, J. M. Villegas and D. P. Rillema, *J. Phys. Chem. B*, 2004, **108**, 12175–12180.

27 X. Zhang, A. M. Wright, N. J. DeYonker, T. K. Hollis, N. L. Hammer, C. E. Webster and E. J. Valente, *Organometallics*, 2012, **31**, 1664–1672.

28 S. R. Stoyanov, C.-X. Yin, M. R. Gray, J. M. Stryker, S. Gusarov and A. Kovalenko, *J. Phys. Chem. B*, 2010, **114**, 2180–2188.

29 D. Herebian, K. E. Wieghardt and F. Neese, *J. Am. Chem. Soc.*, 2003, **125**, 10997–11005.

30 G.-J. Zhao, K.-L. Han and P. J. Stang, *J. Chem. Theory Comput.*, 2009, **5**, 1955–1958.

31 P. Pratihar , T. K. Mondal, A. K. Patra and C. Sinha, *Inorg. Chem.*, 2009, **48**, 2760–2769.

32 S. R. Stoyanov, A. Titov and P. Král, *Coord. Chem. Rev.*, 2009**, 253**, 2852–2871.

33 I. V. Novozhilova, A. V. Volkov and P. Coppens, *J. Am. Chem. Soc.*, 2003, **125**, 1079-1087.

34 (*a*) E. Runge and E. K. U. Gross, Phys. Rev. Lett., 1984, **52**, 997–1000; (*b*) M. E. Casida, C. Jamorski, F. Bohr, J. Guan and D. R. Salahub, in Theoretical and Computational Modeling of NLO and Electronic Materials, edited by S. P. Karna and A. T. Yeates (ACS Press: Washington, D.C., 1996), (Proceedings of ACS Symposium, Washington, D.C., 1994), p. 145.

35 G. S.-M. Tong and C.-M. Chem, *Chem. Eur. J.*, 2009, **15**, 7225 – 7237.

36 A. Y. Sokolov and H. F. Schaefer, *Dalton Trans.*, 2011, **40**, 7571-7582.

37 D. Escudero and W. Thiel, *Inorg. Chem.* 2014, **53**, 11015–11019.

38 (*a*) M. Kaupp, O. Malkina and V. J. Malkin, *J. Chem. Phys.*, 1997, **106**, 9201-9212. (*b*) M. Buchs and C. Daul, *Chimia*, **1998**, *52*, 163-166. (*c*) C. Daul, E. J. Baerends and P. Vernooijs, *Inorg. Chem.*, 1994, **33**, 3538-3543.

39 R. A. Kirgan and D. P. Rillema, *J. Phys. Chem. A*, 2007, **111**, 13157-13162.

40 (*a*) D. M. Dattelbaum, R. L. Martin, J. R. Schoonover and T. J. Meyer, *J. Phys.Chem. A*, 2004, **108**, 3518-3526. (*b*) D. M. Dattelbaum, K. M. Omberg, J. P. Hay, N. L. Gebhart, R. L. Martin, J. R. Schoonover and T. J. Meyer, J. *J. Phys. Chem. A*, 2004, **108**, 3527-3536.

41 S. Frantz, J. Rall, I. Hartenbach, T. Schleid, S. Zalis, and W. Kaim, *Chem. Eur. J.*, 2004, **10**, 149-154.

42 (*a*) L. Yang, A. M. Ren, J. K. Feng, X. J. Liu, Y. G. Ma, M. Zhang, X. D. Liu, J. C. Shen and H. X. Zhang, *J. Phys. Chem. A*, 2004, **108**, 6767-6808. (*b*) J. Dyer, W. J. Blau, C. G. Coates, C. M. Creely, J. D. Gavey, M. W. George, D. C. Grills, S. Hudson, J. M. Kelly, P. Matousek, J. J. McGarvey, J. McMaster, A. W. Parker, M. Towrie and J. A. Weinstein, *Photochem. Photobiol. Sci.*, 2003, **2**, 542-554.

43 H. R. Zhekova, M. Seth and T. Ziegler, *Int. J. Quantum Chem.*, 2014, **114**, 1019−1029.

44 S. D. Cummings and R. Eisenberg, *J. Am. Chem. Soc.*, 1996, **118**, 1949-1960.

45 J. Frey, B. F. E. Curchod, R. Scopelliti, I. Tavernelli, U. Rothlisberger, M. K. Nazeeruddin and E. Baranoff, *Dalton Trans.*, 2014, **43**, 5667-5679.

46 X. Zarate, E. Schott, T. Gomez and R. Arratia-Perez, *J. Phys. Chem. A*, 2013, **117**, 430-436.

47 L. P. Hammett, *J. Am. Chem. Soc.*, 1937, **59**, 96–103.

48 F. A. Carey and R. Sundberg, *Advanced Organic Chemistry Part A and B*, 5th ed., Springer, New York, 2007**.**

49 H. Gilman and H. J. Gaj, *J. Org. Chem.*, 1957, **22**, 447-449.

50 S. A. Gardner, H. B. Gordon and M. P. Rausch, *J. Organomet. Chem.*, 1973, **60**, 179-188.

51 G. B. Kauffman and D. O. Cowan, *Inorg. Synth.*, 1960, **6**, 211-215.

52 A. D. Becke, *J. Chem. Phys.*, 1993, **98**, 5648-5652.

53 (*a*) J. P. Perdew, K. Burke and M. Ernzerhof, *Phys. Rev. Lett.*, 1996, **77**, 3865-3868; (*b*) J. P. Perdew, K. Burke and M. Ernzerhof, *Phys. Rev. Lett.*, 1996, **77**, 3865-3869.

54 (*a*) C. Adamo, M. Cossi and V. Barone, *Theochem*, 1999, **493,** 145-157; (*b*) M. Ernzerhof, and G. E. Scuseria, *J. Chem. Phys.*, 1999, **110**, 5029-5036.

55 J. P. Perdew, in *Electronic Structure of Solids '91*, ed. P, Ziesche, and H. Esching, Akademie Verlag, Berlin, 1991, p. 11.

56 (*a*) J. P. Perdew, J. A. Chevary, S. H. Vosko, K. A. Jackson, M. R. Pederson, D. J. Singh and C. Fiolhais, *Phys. Rev. B*, 1992, **46**, 6671-6687; (*b*) J. P. Perdew, J. A. Chevary, S. H. Vosko, K. A. Jackson, M. R. Pederson, D. J. Singh and C. Fiolhais, *Phys. Rev. B*, 1993, **48**, 4978.

57 (*a*) J. P. Perdew, K. Burke and Y. Wang, *Phys. Rev. B*, 1996, **54**, 16533-16540; (*b*) K. Burke, J. P. Perdew and Y. Wang, in *Electronic Density Functional Theory: Recent Progress and New Directions*, ed. J. F. Dobson, G. Vignale and M. P. Das, Plenum, New York, 1998.

58 Gaussian 03, Revision D.01, M. J. Frisch, G. W. Trucks, H. B. Schlegel, G. E. Scuseria, M. A. Robb, J. R. Cheeseman, J. A. Montgomery, Jr., T. Vreven, K. N. Kudin, J. C. Burant, J. M. Millam, S. S. Iyengar, J. Tomasi, V. Barone, B. Mennucci, M. Cossi, G. Scalmani, N. Rega, G. A. Petersson, H. Nakatsuji, M. Hada, M. Ehara, K. Toyota, R. Fukuda, J. Hasegawa, M. Ishida, T. Nakajima, Y. Honda, O. Kitao, H. Nakai, M. Klene, X. Li, J. E. Knox, H. P. Hratchian, J. B. Cross, V. Bakken, C. Adamo, J. Jaramillo, R. Gomperts, R.E. Stratmann, O. Yazyev, A. J. Austin, R. Cammi, C. Pomelli, J. W. Ochterski, P. Y. Ayala, K. Morokuma, G. A. Voth, P. Salvador, J. J. Dannenberg, V. . Zakrzewski, S. Dapprich, A. D. Daniels, M. C. Strain, O. Farkas, D. K. Malick, A. D. Rabuck, K. Raghavachari, J. B. Foresman, J. V. Ortiz, Q. Cui, A. G. Baboul, S. Clifford, J. Cioslowski, B. B. Stefanov, G. Liu, A. Liashenko, P. Piskorz, I. Komaromi, R. L. Martin, D. J. Fox, T. Keith, M. A. Al-Laham, C. Y. Peng, A. Nanayakkara, M. Challacombe, P. M. W. Gill, B. Johnson, W. Chen, C. Wong, M. W. Gonzalez and J. A. Pople, Gaussian, Inc., Wallingford CT, 2004.

59 (*a*) J. E. Monat, J. H. Rodriguez and J. K. McCusker, *J. Phys. Chem. A*, 2002, **106**, 7399-7406; (*b*) J. H. Rodriguez, D. E. Wheeler and J. K. McCusker, *J. Am. Chem. Soc.*, 1998, **120**, 12051-12068.

60 S. H. Vosko, L. Wilk and M. Nusair, *Can. J. Phys.*, 1980, **58**, 1200-1211.

61 M. Cossi, V. Barone, *J. Chem. Phys.*, 2001, **115**, 4708-4717.

62 (*a*) V. Barone and M. Cossi, *J. Phys. Chem. A*, 1998, **102**, 1995-2001; (*b*) M. Cossi, N. Rega, G. Scalmani and V. Barone, *J. Comput. Chem.*, 2003**, 24**, 669-681.

63 (*a*) I. Mayer, *Chem. Phys. Lett*., 1983, **97**, 270-274; (*b*) I. Mayer, *Int. J. Quantum Chem*., 1984, **26**, 151-154.

64 R. E. Stratmann, G. E. Scuseria and M. J. Frisch, *J. Chem. Phys*, 1998, **109**, 8218-8224.

65 R. Bauernschmitt and R. Ahlrichs, *Chem. Phys. Lett.*, 1996, **256**, 454-464.

66 R. Cammi, B. Mennucci and J. Tomasi, *J. Phys. Chem. A*, 2000, **104**, 5631-5637.

67 S. R. Stoyanov, J. M. Villegas and D. P. Rillema, *Inorg. Chem. Commun.*, 2004, **7***, 838-841.

68 P. M. Kozlowski, J. Kuta, T. Ohta, and T. Kitagawa, *J. Inorg. Biochem.*, 2006**, 100**, 744-750.

69 M. E. Casida, C. Jamorski, K. C. Casida and D. R. Salahub, *J. Chem. Phys.*, 1998, **108**, 4439-4449.

70 (*a*) F. Weigend and R. Ahlrichs, *Phys. Chem. Chem. Phys.*, 2005, **7**, 3297-3305; (*b*) F. Weigend, *Phys. Chem. Chem. Phys.*, 2006*, **8,** 1057-1065.

71 (*a*) Bruker APEX2 User Manual, 2006, Bruker AXS Inc., Madison, Wisconsin, USA; (*b*) G. M. Schdrick, SHELXS97 and SHELXL97, 1997, University of Gottingen, Germany

72 G. M. Brown, H. R. Hopf, T. J. Meyer and D. G. Whitten, *J. Am. Chem. Soc*., 1975, **97**, 5385-5390.

73 D. P. Rillema, J. K. Nagle, L. F. Barringer, Jr. and T. J. Meyer, *J. Am. Chem. Soc.*, 1981, **103**, 56-62.

74 J. M. Villegas, S. R. Stoyanov and D. P. Rillema, *Inorg. Chem.*, 2002, **41**, 6688-6694.

75 G. Zhang and C. B. Musgrave, *J. Phys. Chem. A*, 2007, **111**, 1554-1561.

76 W. A. Tarran, G. R. Freeman, L. Murphy, A. M. Benham, R. Iataky and J. A. G. Williams, *Inorg. Chem*, 2014. **53**, 5738-5749.

77 C. E. Wittle, J. A. Weinstein, M. W. George and K. Schanze, *Inorg. Chem.*, 2001, 40, 4053-4062.